Tri-Band Patch Array Antenna Design for 5G Medical Data Communication in Sub-6 GHz and mmWave Bands

Paleerat Wongchampa and Lerson Kirasamuthranon*

Department of Electronics Engineering Technology, College of Industrial Technology,
King Mongkut’s University of Technology, North Bangkok, Thailand
Email: paleeratw@kmutnb.ac.th (P.W.); lersonk@kmutnb.ac.th (L.K.)
*Corresponding author

Abstract**—This paper presents the design and validation of a tri-band patch array antenna intended for 5G-based medical data communication. The proposed antenna operates efficiently across 0.7 GHz, 2.6 GHz (sub-6 GHz), and 26 GHz (mmWave), aligning with the 5G spectrum allocations used in Thailand. The antenna’s T–F shaped single-patch structure is optimized to achieve impedance matching, high gain, and radiation efficiency across all three bands. Simulations in CST Microwave Studio were performed to evaluate |S11|, gain, and efficiency across different array configurations (2×1, 2×2, 4×1, and 4×2). Based on these results, the 2×2 array was selected for prototype fabrication and experimental testing. The fabricated prototype was characterized using a Vector Network Analyzer and radiation pattern measurements in a controlled indoor setup. Furthermore, an over-the-air communication test using USRP software-defined radios was conducted to measure Packet Error Rate (PER) and Signal-to-Interference-plus-Noise Ratio (SINR) at different distances. Results demonstrated that the 2×2 array significantly outperformed the single-element antenna, with lower PER and higher SINR at both 0.7 and 2.6 GHz. The proposed antenna, designed for non-implantable, device-level integration, is well suited for applications such as remote patient monitoring and medical IoT. Its tri-band capability ensures reliable connectivity across multiple 5G layers, while its compact design enables integration into portable medical devices. Future work will extend to hybrid beamforming and full 5G link validation including BER and latency analysis.**

Keywords**— antenna array, 5G, microstrip antenna, medical communication, tri-band**

I. INTRODUCTION

5G wireless technology is rapidly transforming many industries, including healthcare [1]. With growing demand for real-time medical services, remote monitoring, and IoMT devices, reliable multi-band antennas are essential to ensure seamless connectivity [2–5]. 5G offers low latency and high reliability Ultra-Reliable Low Latency Communications (URLLC) as well as high-speed connectivity Enhanced Mobile Broadband (eMBB), well suited for medical applications [6–8]. However, wireless links in hospital environments still face challenges such as interference, multipath fading, and efficient spectrum utilization [9–11]. According to 3GPP standards [12–14], healthcare use cases-ranging from remote surgery to ambulance-to-hospital communication-require both sub-6 GHz bands for coverage and mobility, and mmWave bands for high-capacity data transfer.

In this context, the proposed antenna is designed for non-implantable, device-level integration in medical IoT systems, particularly for remote patient monitoring applications. As illustrated in Fig. 1, physiological sensors such as ECG, heart rate, blood pressure, oxygen saturation, EMG, and temperature collect patient data and transmit it to a portable medical gateway equipped with the proposed T–F tri-band antenna. The gateway then communicates with healthcare centers and medical personnel over multi-layer 5G networks, leveraging sub-GHz, sub-6 GHz, and mmWave bands to ensure reliable connectivity under diverse indoor propagation conditions.

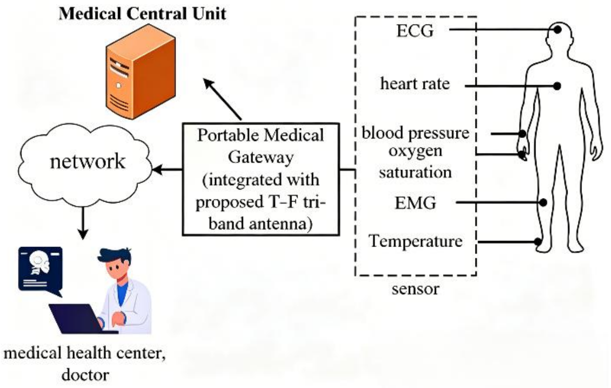

Fig. 1. Conceptual integration of the proposed T–F tri-band antenna in a non-implantable portable medical gateway for medical IoT applications.

Microstrip patch antennas are widely adopted due to their low profile, ease of integration, and cost-

---

Manuscript received October 18, 2025; revised January 20, 2026; accepted February 5, 2026; published May 13, 2026.

doi:10.12720/jcm.21.3.351-364

effectiveness [15, 16]. Techniques such as slotting, geometry tuning, and Defected Ground Structures (DGS) have been used to achieve multiband operation [17, 18]. Yet few designs support concurrent sub-6 GHz and mmWave operation in compact, low-cost formats suitable for portable medical devices.

Recent studies have explored tri-band and hybrid multi-band antennas for IoT and 5G applications. Rahman et al. [19] proposed a 3×2 MIMO antenna on Rogers RT/duroid 5880 with wide bandwidths across sub-6, Ku, and mmWave bands, but with high structural complexity, no sub-GHz coverage, and no OTA validation. Rahman [20] introduced a tri-band integrated MIMO design using metamaterial/metasurface loading, achieving high isolation and gain, but limited to microwave and mmWave bands without Over-The-Air (OTA) performance evaluation. Sharma [21] presented a flexible four-port MIMO antenna operating exclusively in the FR2 mmWave bands, demonstrating high isolation and SAR compliance, yet lacking sub-6 GHz or sub-GHz support. Singh [22] realized a compact FR-4 Y-slot patch antenna with defected ground structure (DGS) for tri-band sub-6 GHz operation, though the efficiency was constrained and no mmWave functionality was included.

More recently, hybrid sub-6 GHz and mmWave antenna designs implemented on low-cost FR-4 substrates have been reported, demonstrating dual-band operation and measured performance at both frequency ranges [23]. In parallel, medical and wearable antenna studies have focused on mmWave bands with strong emphasis on radiation efficiency and SAR compliance, but are typically limited to mmWave-only operation without concurrent sub-6 GHz coverage or OTA-based link validation [24].

Table I summarizes these representative works. While each design demonstrates specific merits, none simultaneously supports sub-GHz, sub-6 GHz, and mmWave bands within a compact FR-4 platform while also providing experimental OTA reliability validation.

TABLE I. COMPARISON OF RECENT TRI-BAND ANTENNA DESIGNS FOR IOT AND 5G APPLICATIONS

Work	Bands Coverd	Substrate / Structure	Geometry / Approach	Key Results	Limitations
Proposed T-F Tri-band Array (This Work)	0.7 GHz (sub-GHz), 2.6 GHz (sub-6), 26 GHz (mmWave)	FR-4 (low-cost, practical)	Novel T–F patch + 2×2 array, simple fabrication	Compact, concurrent sub-GHz + mmWave coverage, stable gain, >70% eff. (sim), OTA PER/SINR validation for reliability	Efficiency measured only by sim, OTA limited to 0.7/2.6 GHz
[19]	Sub-6 GHz (2–7 GHz), Ku (13–17.5 GHz), mmWave (24.5–38.2 GHz)	Rogers RT/duroid 5880	Multi-slot patch array with reflector, ML-aided gain prediction	Wide bandwidth (111%, 29.5%, 43.7%), strong isolation (ECC < 0.004), DG ≈ 10 dB	High design complexity, no sub-GHz coverage, no OTA PER/SINR validation
[20]	Microwave (2.6–4.1, 5.3–11.3 GHz), mmWave (22.5–29.3 GHz)	Rogers RT/duroid 5880	Integrated tri-band MIMO with MTM meta surface loading	High isolation (27–40 dB), gain up to 11 dBi at 28 GHz, eff. 70–87%, ECC < 0.0002, DG ≈ 10 dB	No sub-GHz support, design complexity, OTA not reported
[21]	mmWave: 27.8, 32.0, 37.4 GHz	Rogers RT/duroid 5880 (flexible)	Four-port flexible MIMO with parasitic isolation	Isolation >30 dB, ECC < 0.001, DG = 10 dB, SAR < 1.6 W/kg, bending-resilient	mmWave-only, no sub-6 or sub-GHz coverage
[22]	Sub-6 GHz tri-band (~0.9, 2.4, 3.5–5.8 GHz)	FR-4 with DGS	Compact Y-slot patch + defected ground	Small size, simple geometry, S11 < –10 dB at 3 bands	No mmWave, efficiency limited by FR-4 loss tangent, OTA not reported
[23]	Sub-6 (3.5 GHz), 26 GHz mmWave	FR-4 (low-cost)	Integrated dual-band antenna array modules	Wide bandwidth at both bands, measured performance on FR-4	Not tri-band, no OTA validation
[24]	mmWave (28, 38 GHz)	Rogers / wearable	Compact wearable dual-band antenna with SAR compliance	High gain & efficiency, SAR tested	mmWave-only, no sub-6/sub-GHz, no OTA validation

In contrast, the proposed T–F shaped patch antenna simultaneously operates at 0.7, 2.6, and 26 GHz in a compact, low-cost FR-4 configuration and uniquely incorporates OTA performance assessment through PER and SINR measurements, addressing both practical deployment and reliability requirements for 5G medical IoT systems. Unlike conventional multi-slot or Defected Ground Structure (DGS)-based techniques commonly used to realize multi-band microstrip antennas, the proposed T–F-shaped radiator achieves tri-band operation through distinct current paths within a single compact patch element. Multi-slot designs typically require multiple etched slots on the radiating surface, while DGS approaches rely on perturbations in the ground plane to introduce additional resonant modes. Although effective in bandwidth enhancement, these techniques often increase fabrication complexity and can degrade radiation efficiency, particularly at mmWave frequencies when implemented on FR-4 substrates.

To overcome these limitations, the proposed T–F geometry preserves an intact ground plane and exploits the horizontal "T" section and vertical "F" extension to support the 0.7 GHz, 2.6 GHz, and 26 GHz resonances through physically separated and independent current paths. This approach reduces sensitivity to fabrication tolerances, improves practical efficiency, and facilitates straightforward extension to array configurations. As a result, the antenna provides concurrent sub-GHz, sub-6 GHz, and mmWave operation in a compact, low-cost structure suitable for 5G medical IoT applications.

In this paper, we present the design, optimization and experimental validation of a compact tri-band patch antenna array aligned with Thailand's 5G spectrum allocations. A novel T–F shaped radiator is introduced to achieve concurrent sub-GHz, sub-6 GHz, and mmWave operation. The antenna was optimized in CST Microwave Studio, fabricated on FR-4, and validated through return loss, gain, radiation patterns, and OTA link performance. This work targets non-wearable 5G medical devices such as smart ambulance gateways and portable monitors and establishes a foundation for hybrid beamforming integration and full-system evaluation including BER and latency in realistic 5G environments.

The motivation for selecting a T-F shaped geometry lies in its ability to support compact multi-band operation using distinct current paths. The T-shaped structure offers an extended current path, ideal for low-frequency resonance (0.7 GHz), while the F-shaped extension introduces additional branches that support mid-and high-frequency operation through harmonic resonance and coupling. This geometry enables the antenna to achieve tri-band operation without requiring additional radiators or substrate area.

II. ANTENNA DESIGN, SIMULATION AND ARRAY EXTENSION

This section introduces the design methodology of a compact antenna capable of operating effectively in three frequency bands: 0.7 GHz, 2.6 GHz, and 26 GHz. The design was aligned with the 5G spectrum allocations in Thailand, with the aim of improving the efficiency and reliability of wireless medical communication. The overall process began with analytical calculations based on classical microstrip patch theory, followed by geometry refinement, full-wave simulation, and experimental validation.

A. Single-Element Antenna Design

The proposed tri-band single-element antenna is modeled using CST Microwave Studio and designed to satisfy a 50-ohm impedance matching requirement. The structure consists of a T–F shaped patch radiator, a ground plane, and a microstrip feed line. FR-4 is selected as the substrate material due to its low cost, wide availability, and suitability for compact multi-band antenna design. The substrate has a dielectric constant (εr) of 4.3 and a thickness of 1.6 mm.

Although FR-4 offers practical advantages, its dielectric loss tangent is frequency-dependent, increasing from approximately 0.0035 at sub-6 GHz to about 0.02 at 26 GHz. This increased loss leads to reduced radiation efficiency at mmWave frequencies. Nevertheless, this trade-off is acceptable for a proof-of-concept prototype. Low-loss substrates such as Rogers RO4350B or RT/duroid 5880 could provide an efficiency improvement of approximately 10–15% at 26 GHz and are considered for future work.

Initial patch dimensions were estimated using standard microstrip patch equations. The resonant length of the fundamental mode was approximated as:

$$L \approx \frac{c}{2 f_r \sqrt{\varepsilon_{eff}}} \tag{1}$$

where c is the speed of light, f_r is the target resonant frequency, and $\varepsilon_{\mathrm{eff}}$ is the effective dielectric constant. The effective permittivity and length extension (ΔL) were computed following conventional formulas for microstrip patches. These equations were applied to the three target frequencies (0.7, 2.6, and 26 GHz) to obtain baseline dimensions, which were later refined through simulation.

Fig. 2(a) shows the top view of the proposed antenna, which consists of the hybrid T-F radiating structure and the feedline. The back side includes the ground plane as shown in Fig. 2(b), which aids in reducing interference and improving radiation performance. The antenna was designed to achieve operation at 0.7 GHz, 2.6 GHz, and 26 GHz, covering both sub-6 GHz and mmWave bands suitable for 5G-based medical communication.

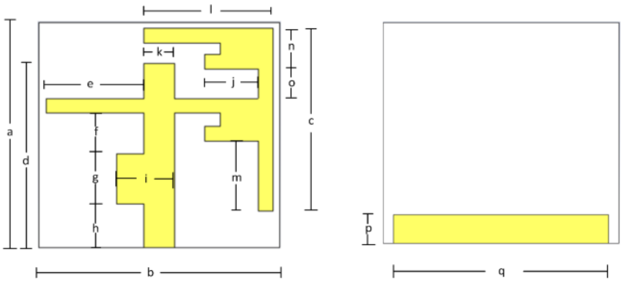

(a) (b)

Fig. 2. Proposed single-element antenna design: (a) Front, (b) ground plane.

Unlike conventional multi-slot and Defected Ground Structure (DGS) techniques that are widely employed to realize multi-band operation, the proposed T–F geometry achieves tri-band performance within a single compact radiator. Multi-slot patches require multiple etched slots on the patch surface, increasing footprint and fabrication complexity, while DGS methods perturb the ground plane, which often introduces parasitic coupling and higher loss at mmWave frequencies, particularly on FR-4 substrates. Recent works have confirmed that DGS and multi-slot approaches can enhance bandwidth but at the expense of efficiency and manufacturability [25–27].

The T–F shaped geometry enables compact tri-band operation by exploiting distinct current paths. The horizontal T-shaped section provides an extended current path suitable for sub-GHz resonance, while the vertical F-shaped extension introduces additional branches that support mid-band and mmWave operation through coupling and higher-order modes.

Fig. 3 (a)–(c) illustrates the simulated surface current distributions at 0.7, 2.6, and 26 GHz, respectively. The results confirm that different current paths are selectively excited at each frequency, validating the effectiveness of the proposed T–F radiator in achieving compact tri-band operation without enlarging the antenna footprint or modifying the ground plane.

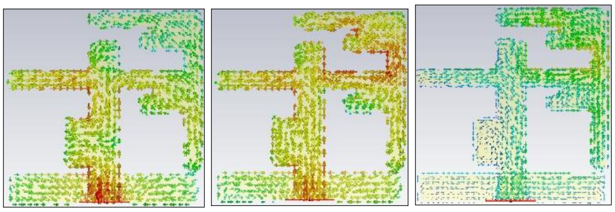
(a) (b) (c)

Fig. 3. Simulated surface current distributions of the proposed T–F radiator at: (a) 0.7 GHz, (b) 2.6 GHz, and (c) 26 GHz, showing distinct current paths responsible for tri-band operation.

Based on the physical insight provided by the surface current analysis and the frequency contribution summarized in Table II, a parametric sweep was performed to quantitatively investigate the sensitivity of the antenna response to key geometrical parameters. In particular, the coupled parameters m and l, which define the effective length of the vertical F-shaped stub, were varied simultaneously to examine their impact on the 2.6 GHz resonance. Fig. 4 shows the simulated |S11| responses for different combinations of m and l, demonstrating a clear tuning of the 2.6 GHz resonance while maintaining a narrow impedance bandwidth and minimal influence on the other operating bands.

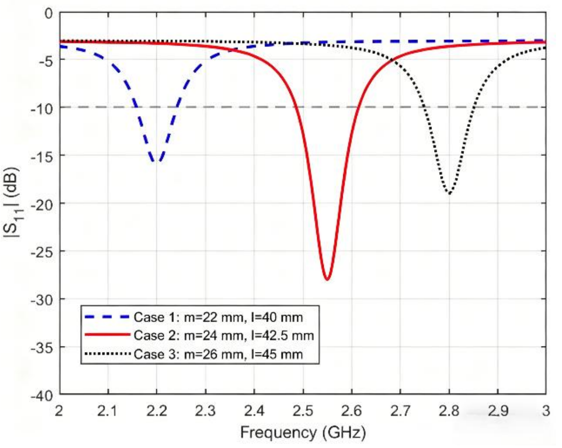

Fig. 4. Parametric sweep of m and l showing the tuning of the 2.6 GHz resonance.

B. Simulation Results and Parametric Optimization of the Single Element

Full-wave electromagnetic simulations were performed in CST Microwave Studio using a frequency-domain solver with wave-port excitation. Key performance metrics, including reflection coefficient (S11), realized gain, and radiation efficiency, were evaluated at 0.7, 2.6, and 26 GHz. Based on the surface current analysis and the frequency contribution summarized in Table II, a parametric sweep was conducted to investigate the sensitivity of the antenna response to key geometrical parameters. In particular, the coupled parameters m and l, which define the effective length of the vertical F-shaped stub, were varied simultaneously to examine their impact on the 2.6 GHz resonance. Fig. 4 shows the simulated |S11| responses for different combinations of m and l, demonstrating clear tuning of the 2.6 GHz resonance while maintaining narrow impedance bandwidth and minimal influence on the other operating bands.

TABLE II. FREQUENCY CONTRIBUTION OF KEY STRUCTURAL ELEMENTS

Frequency (GHz)	**Primary Geometry Component**	**Resonance Mechanism**
0.7	Long horizontal arm of T	Quarter-wavelength current path
2.6	Vertical stub of F	Slot coupling and higher-order mode
26	Shorted side branches of F	Self-resonant harmonic tuning

TABLE III. DESIGN PARAMETERS OF THE PROPOSED T–F SHAPED ANTENNA

Parameter	**Length (mm)**	**Parameter**	**Length (mm)**	**Parameter**	**Value**
a	77	j	17.5	Substrate	FR-4
b	79	k	10	Substrate thickness	1.6 mm
c	62.5	l	42.5	Feedline width	10 mm
d	63	m	24	Feedline length	15mm
e	32	n	14	Ground plane size	10 × 72 mm^2
f	14	o	10	Copper thickness	35 µm
g	17	p	10		
h	15	q	72		
i	19				

During the design process, a goal-driven optimization was applied within CST Microwave Studio. Initial dimensions were derived from standard microstrip patch equations and subsequently refined through parametric tuning to satisfy the impedance matching criterion ($|S11| < -10$ dB) at all three target frequencies, while preserving structural compactness and manufacturability. The complete geometric, substrate, and feeding parameters of the optimized T–F shaped antenna are summarized in Table III. These parameters were obtained through iterative parametric tuning and frequency-domain full-wave simulations conducted in CST Microwave Studio to ensure proper impedance matching and stable tri-band operation. The inclusion of substrate properties, feedline dimensions, and ground-plane size enables full reproducibility of the proposed design and facilitates its practical implementation in compact medical IoT devices operating over multi-layer 5G networks.

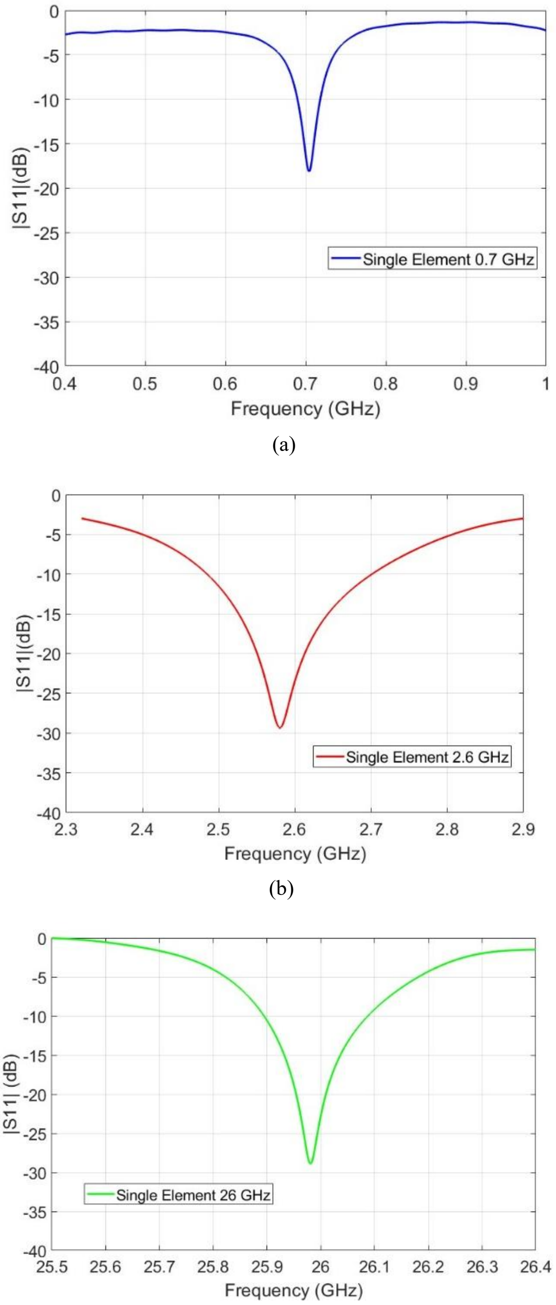

(a)

(b)

(c)

Fig. 5. Simulated S11 of the proposed single-element antenna at: (a) 0.7 GHz, (b) 2.6 GHz, and (c) 26 GHz.

Fig. 5 shows the simulated S11 of the proposed single-element antenna. At 0.7 GHz, the resonance achieves S11 ≈ –18 dB, confirming strong impedance matching for sub-6 GHz medical applications. At 2.6 GHz, the resonance deepens to approximately –28 dB, ensuring stable mid-band operation. At 26 GHz, the antenna maintains efficient matching with S11 ≈ –29 dB, demonstrating consistent mmWave performance.

Fig. 6 presents the realized gain and radiation efficiency. At 0.7 GHz, the antenna achieves 3.23 dB gain with ~64.2% efficiency. At 2.6 GHz, the gain increases to 5.45 dB with ~64.4% efficiency. At 26 GHz, the antenna achieves 3.92 dB gain with ~60% efficiency, which is satisfactory considering the higher dielectric and propagation losses at mmWave.

Overall, the simulation results confirm that the proposed T–F antenna provides robust tri-band operation with strong impedance matching, stable gain, and consistent radiation efficiency across all three frequency bands, making it suitable for 5G medical IoT applications.

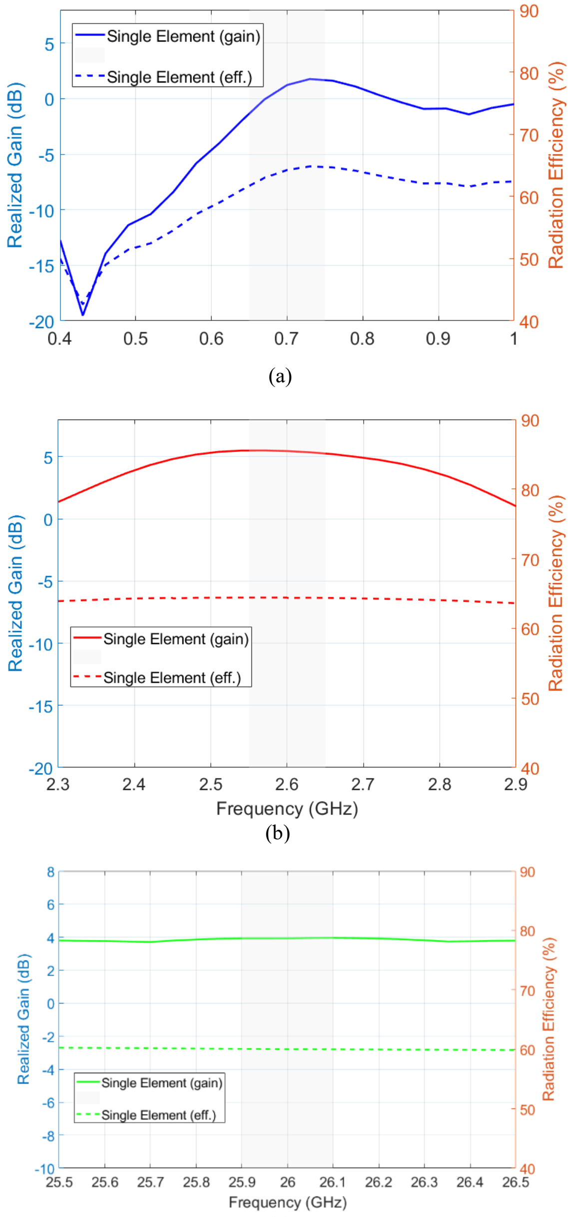

(a)

(b)

(c)

Fig. 6. Simulated realized gain (left axis) and radiation efficiency (right axis) of the single-element antenna at: (a) 0.7 GHz, (b) 2.6 GHz, and (c) 26 GHz. Solid lines represent realized gain, while dashed lines represent radiation efficiency.

C. Multi-element Array Configuration and Evaluation

To enhance gain and directivity beyond the limitations of a single element, the proposed radiator was extended into multi-element array configurations. Four array layouts (2×1, 2×2, 4×1, and 4×2) were designed and simulated in CST Microwave Studio. The inter-element spacing was set to approximately $\lambda/2$ at 2.6 GHz to balance mutual coupling and radiation performance in the mid-band.

Because the spacing is defined relative to 2.6 GHz, the same physical separation corresponds to a much larger electrical spacing at 26 GHz (approximately 5λ), which can lead to narrower main beams and increased sidelobe/grating-lobe tendencies at mmWave frequencies. This behavior is consistent with array-factor considerations and indicates that the present configuration is not optimized for mmWave beam steering.

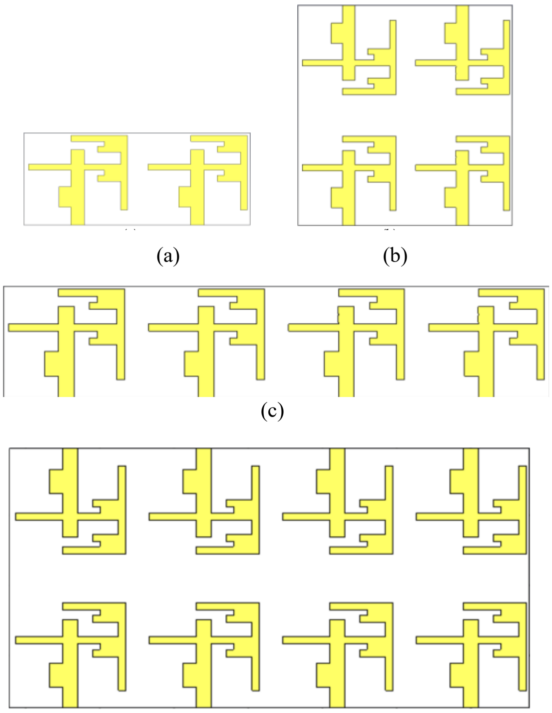
(a) (b)

(c)

(d)

Fig. 7. Proposed array antenna design: (a) 2×1 (b) 2×2 (c) 4×1 (d) 4×2.

Nevertheless, the simulated results remain suitable for proof-of-concept tri-band operation. Future work will investigate mmWave-oriented array layouts with reduced spacing ($\leq \lambda/2$ at 26 GHz) and/or hybrid beamforming sub-array architectures to suppress grating lobes and improve directivity. All arrays employed a corporate-feed network with uniform amplitude and phase excitation. The physical layouts of the four configurations are shown in Fig. 7.

Fig. 8 presents the simulated S11 results. At 0.7 GHz, all configurations achieve strong impedance matching (S11 < –20 dB), with the 2×2 and 4×2 arrays exhibiting the lowest reflection levels. At 2.6 GHz, the 2×2 array shows the deepest resonance (≈ –35 dB), while the other arrays maintain satisfactory matching (S11 < –15 dB).

At 26 GHz, all configurations remain below –10 dB, with the 2×2 and 4×2 arrays again providing strong impedance matching.

Fig. 9(a)–(c) present the simulated realized gain (left axis) and radiation efficiency (right axis) of the 2×1, 2×2, 4×1, and 4×2 array configurations at 0.7, 2.6, and 26 GHz. At 0.7 GHz, the 2×2 array achieves the best overall performance, with a peak gain close to 5 dB and radiation efficiency exceeding 75%. The 4×1 and 4×2 arrays exhibit comparatively lower gain and efficiency, which can be attributed to increased coupling and less favorable current distribution at the sub-GHz band. At 2.6 GHz, all array configurations maintain stable gain values of approximately 4.5–5.5 dB, with radiation efficiency above 68%, indicating consistent mid-band performance. At 26 GHz, the realized gain remains within 4–5 dB and the radiation efficiency remain above 65% for all configurations, despite the increased dielectric loss of the FR-4 substrate at mmWave frequencies.

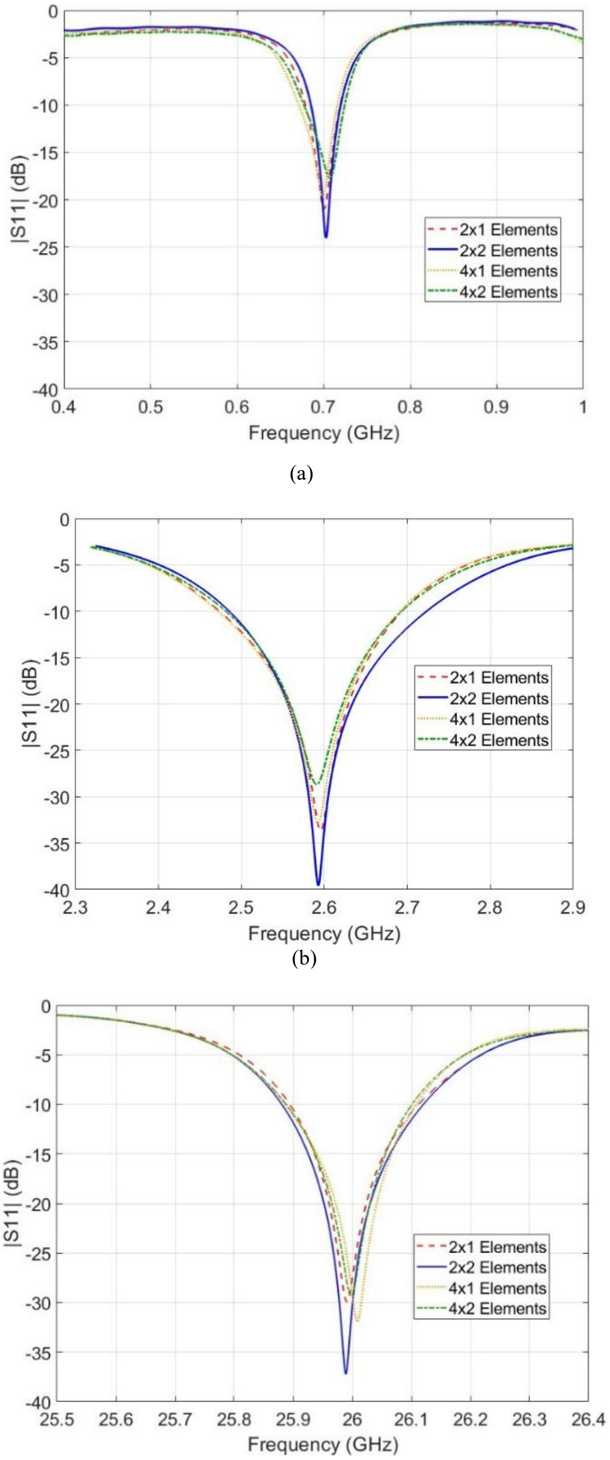

(a)

(b)

(c)

Fig. 8. S11 of 2×1, 2×2, 4×1, and 4×2 array antennas at: (a) 0.7 GHz, (b) 2.6 GHz, (c) 26 GHz.

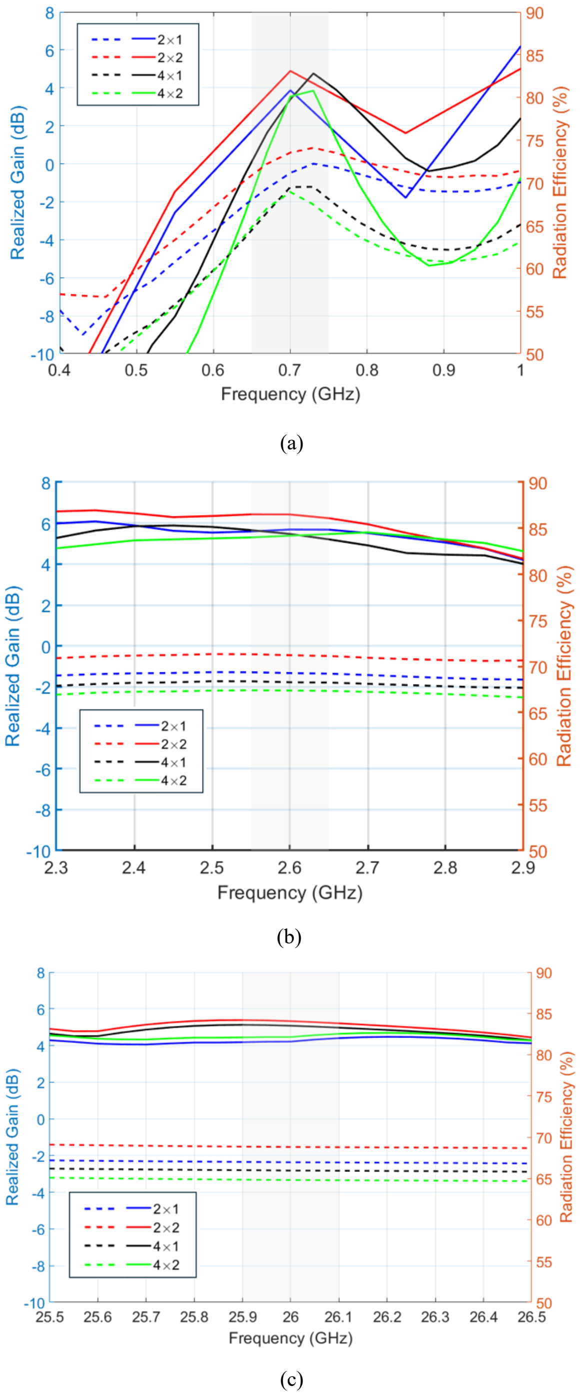

(a)

(b)

(c)

Fig. 9. Simulated realized gain (left axis) and radiation efficiency (right axis) of 2×1, 2×2, 4×1, and 4×2 array configurations at: (a) 0.7 GHz, (b) 2.6 GHz, and (c) 26 GHz. Solid lines represent realized gain, while dashed lines represent radiation efficiency.

Overall, the 2×2 configuration provides the best trade-off between electrical performance and compactness. Therefore, the 2×2 array was selected for prototype fabrication and implemented using a 4-to-1 corporate combiner as a single-port array for experimental validation, rather than a multi-port MIMO antenna.

III. MEASUREMENT RESULTS OF THE FABRICATED 2×2 ANTENNA ARRAY

A. Experimental Performance Validation of the 2×2 Antenna Array

Based on the simulation results, the 2×2 array provides the best overall trade-off among impedance matching, gain, and radiation efficiency across the three target frequency bands. Therefore, this configuration was selected for prototype fabrication and experimental validation.

The fabricated 2×2 T–F patch array was characterized using a Rohde & Schwarz Vector Network Analyzer (VNA). Prior to measurement, a standard SOLT (short–open–load–through) calibration was performed to ensure accuracy across the full frequency range of interest. The four radiating elements were connected through a 4-to-1 power combiner, resulting in a single RF port interface to the VNA

Fig. 10 illustrates the measurement setup: (a) the fabricated prototype mounted vertically and connected to the VNA via coaxial cables, and (b) a simplified schematic diagram showing the array–combiner–VNA connection. This configuration was used to obtain the S-parameters, particularly |S11|, at 0.7, 2.6, and 26 GHz. The inclusion of both the actual setup and schematic diagram enhances clarity, validates the simulated methodology, and ensures reproducibility of the procedure.

The measured S11 results of the 2×2 array antenna prototype *is* shown in Fig. 11(a)-(c). Clear resonances were observed with |S11| ≈ –13 dB at 0.7 GHz, –22 dB at 2.6 GHz, and –26 dB at 26 GHz, all of which are below the –10 dB threshold, indicating satisfactory impedance matching. A small deviation at 0.7 GHz was noted compared with the simulation (~40 MHz shift), which can be attributed to fabrication tolerances in patch/feedline dimensions, parasitic effects of the SMA connector and soldering, and variations in the dielectric properties of FR-4. These effects are more pronounced at the lowest band due to the larger guided wavelength. Nevertheless, the deviation remains within acceptable tolerance for prototyping, and the measured performance closely follows the simulated trend, confirming robust tri-band operation. Overall, the results validate that the antenna is suitable for practical implementation in medical IoT scenarios.

Fig. 12 shows the laboratory setup used to measure the radiation patterns of the fabricated tri-band antennas. In this experiment, the single-element antenna was used as the transmitter, while the receiving side was alternately configured with the 2×2 array to evaluate and compare their radiation patterns. The transmitting and receiving antennas are installed on a stable support platform and connected with low-loss coaxial cables. The radiation pattern analysis instruments were employed to conduct measurements in a controlled indoor laboratory environment, as shown on the screen. The receiving antennas were rotated or repositioned as necessary to record the radiation characteristics in the azimuth plane.

This configuration provided the opportunity to evaluate the overall radiation efficacy, lobe structure, and beam direction in all three target frequency bands—0.7 GHz, 2.6 GHz, and 26 GHz.

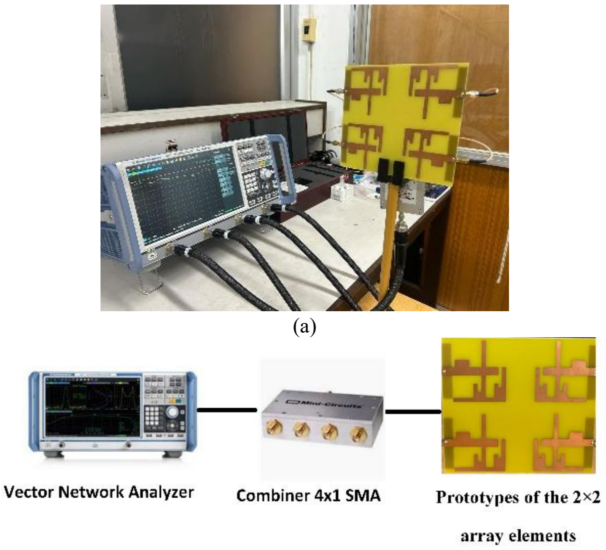

(a)

(b)

Fig. 10. Measurement setup of the 2×2 T–F patch array: (a) Fabricated prototype of the 2×2 T–F patch array connected to the VNA. (b) Simplified schematic diagram of the measurement setup.

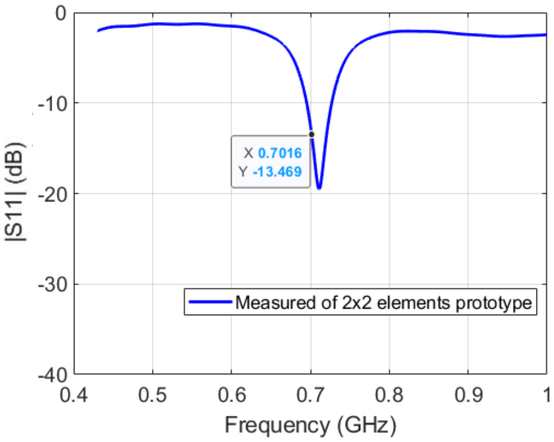

(a)

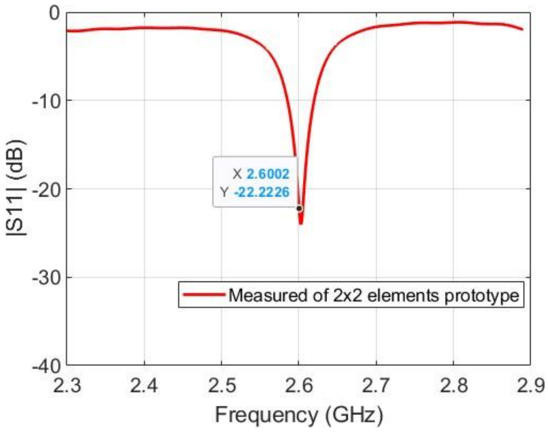

(b)

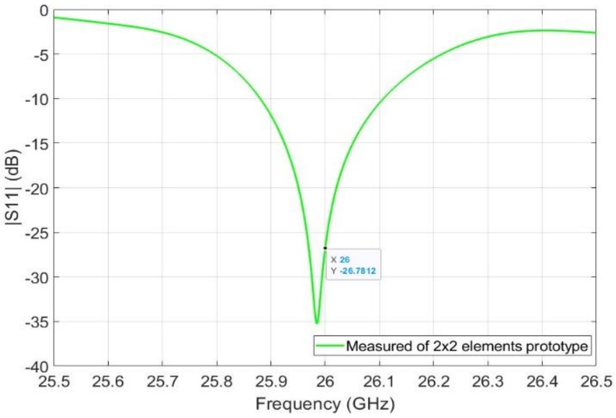

(c)

Fig. 11. Measured return loss of the antenna prototype at: (a) 0.7 GHz (b) 2.6 GHz (c) 26 GHz.

The measured normalized radiation patterns of the 2×2 antenna element prototype at the three designated frequency bands are illustrated in Fig. 13(a)–(c), corresponding to 0.7 GHz, 2.6 GHz, and 26 GHz, respectively. These frequencies are important for sub-6 GHz and mm-Wave 5G communication. The radiation patterns show that the prototype achieves directive radiation in all three bands, but the configuration of the lobes and the main beam orientation differ. At 0.7 GHz and 2.6 GHz, the main lobes are relatively wide, enabling broad coverage suitable for close-range or quasi-omnidirectional communication. At 26 GHz, the radiation becomes more directive with narrower lobes, which is advantageous for line-of-sight links at mm-Wave frequencies. In terms of polarization performance, the co-polarization dominates across all bands, with cross-polarization generally suppressed by more than 10 dB. The suppression is strongest at 2.6 GHz (>15 dB), while at 26 GHz multiple lobes appear due to higher-order mode excitation, but the cross-polarization remains lower than the co-polarization level. It should be noted that the measurements were carried out without an anechoic chamber, and thus some pattern distortions may be attributed to environmental reflections. Nevertheless, the measured co-/cross-polarization trends confirm that the antenna maintains acceptable polarization purity and stable radiation behavior across all three frequency bands.

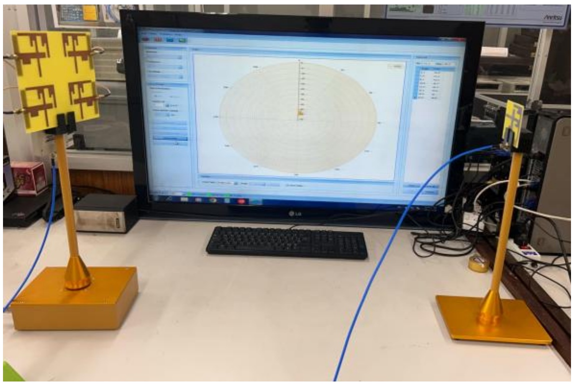

Fig. 12. Experimental setup for radiation pattern measurement of the fabricated 2×2 array elements prototype.

Overall, the measured results confirm that the proposed 2×2 antenna array design performs reliably across all three targeted 5G bands. The gain, bandwidth, and radiation pattern characteristics demonstrate its suitability for integration into real-world 5G medical communication systems.

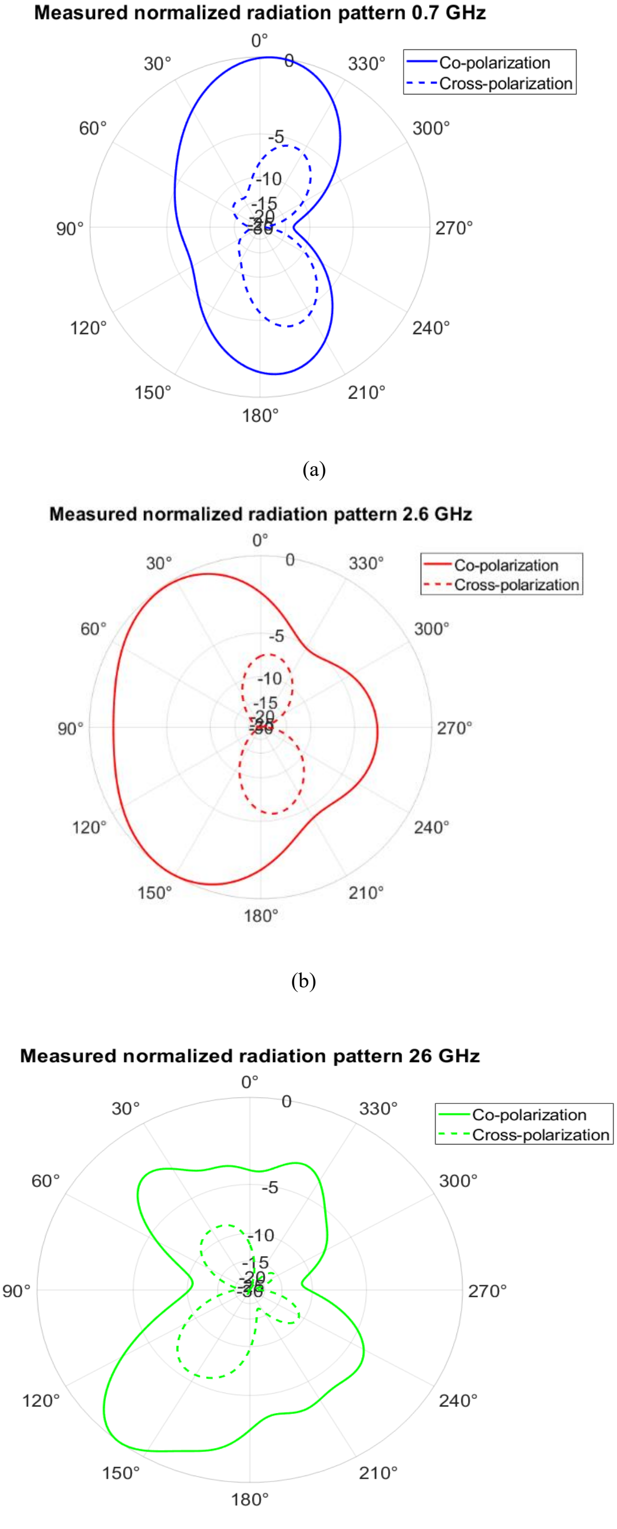

(a)

(b)

(c)

Fig. 13. Measured normalized radiation patterns of the 2×2 antenna prototype at: (a) 0.7 GHz, (b) 2.6 GHz, and (c) 26 GHz, showing co- and cross-polarization.

B. Over-the-Air Link Evaluation Using USRP

To assess the practical communication capability of the proposed antenna design, an Over-the-Air (OTA) evaluation was conducted using Universal Software Radio Peripheral (USRP). This experimental setup emulates a short-range 5G communication link and enables a direct performance comparison between the single-element antenna and the 2×2 antenna array in terms of signal quality and transmission reliability. Key metrics such as Packet Error Rate (PER) and Signal-to-Interference-plus-Noise Ratio (SINR) were measured under controlled indoor conditions. The antennas were configured in a Line-of-Sight (LoS) setup with varying distances between transmitter and receiver—0.5 to 3 meters, incremented by 0.5 meter for each test case. This distance variation aimed to investigate the impact of propagation range and multipath conditions on system performance. The 2×2 array antenna and single element were deployed on the receiver side, while the single-element antenna served as the transmitter. Both antennas were fabricated from the same tri-band design. Transmission parameters were configured as shown in Table IV.

TABLE IV. USRP SET UP PARAMETERS

Modulation Type	BPSK
Data rate	1 Mbps
Frequency	0.7, 2.6 GHz
Packet payload size	20000 Bytes
Packets per trial	1000
Number of data Subcarriers	48
Number of Cyclic Prefix	4
Total subcarrier	52
Transmit Power	+10 dBm
USRP RF Front-End Gain	Tx: 20 dB, Rx: 10 dB
Channel Environment	Indoor LoS, 8×4×3 m³ lab with multipath reflections (walls, metallic furniture)
Separation Distance	0.5–3 m (step 0.5 m)
Test Repetitions	5 trials per distance for averaging

Over-the-Air (OTA) experiments at 0.7 GHz and 2.6 GHz were performed using identical baseband configurations to ensure a fair comparison across frequency bands. In both cases, BPSK modulation, a data rate of 1 Mbps, identical packet payload size, subcarrier allocation, and bandwidth settings were applied, with the carrier frequency being the only variable.

For each antenna configuration and transmission distance, five independent measurement trials were conducted, each consisting of 1,000 transmitted packets. The reported PER and SINR values represent the average across these trials. The observed standard deviation was small relative to the mean values, indicating good repeatability and statistical stability under the controlled indoor environment.

Timing and frequency synchronization between the transmitting and receiving USRP units were handled using the internal USRP reference clock and preamble-based synchronization at the baseband level. Given the short-range line-of-sight indoor setup and stable hardware configuration, residual synchronization errors and frequency offsets were minimal and did not significantly affect the reported PER and SINR trends.

The transmitter output power was set to +10 dBm with the USRP RF front-end gain fixed at 20 dB, while the receiver gain was set to 10 dB. Both antennas were mounted and aligned in boresight under line-of-sight conditions. The experiments were conducted inside an 8× 4×3m³ room located in Building 62, Department of Electronics Engineering Technology, KMUTNB, which included metallic furniture and partitions that introduced typical indoor multipath reflections. For each distance point, 1,000 PRBS packets (payload 20,000 bytes) were transmitted and the PER/SINR values were averaged over five repeated trials to ensure statistical reliability.

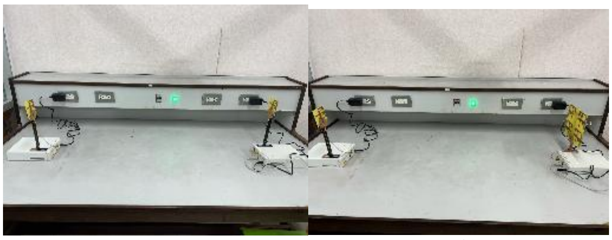

(a) (b)

Fig. 14. Experimental setup for over-the-air 5G communication tests using USRP: (a) Single-element antenna configuration. (b) 2×2 array antenna used as the receiver.

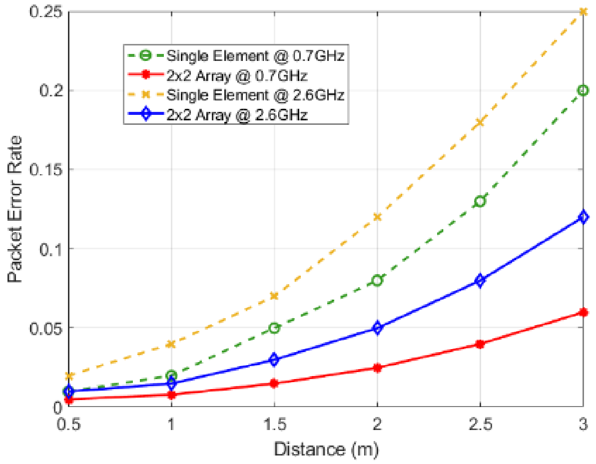

Fig. 15. Measured PER as a function of transmission distance at 0.7 and 2.6 GHz for both the single-element and 2×2 antenna configurations.

Each USRP was connected to a host computer to enable real-time acquisition of PER and SINR values across different distances. Fig. 14 illustrates the experimental testbed layout used in the measurements.

Fig. 15 presents the measured PER of the proposed antennas across varying transmission distances, from 0.5 to 3 meters, for two operating frequencies: 0.7 GHz and 2.6 GHz. The results clearly show that the 2×2 antenna array consistently outperforms the single-element antenna in terms of error performance. At all tested distances, the 2×2 configuration exhibits a significantly lower PER, confirming its advantage in spatial diversity and improved gain. This advantage becomes more pronounced as the distance increases, where the array's enhanced radiation characteristics help maintain better signal integrity.

Moreover, the 0.7 GHz band shows lower PER values compared to 2.6 GHz for both antenna configurations. This is expected, as lower frequencies generally experience less propagation loss and better penetration through obstacles, which aligns with the characteristics of indoor medical communication environments.

As distance increases, the PER also rises for both configurations. This trend highlights the impact of path loss and multipath fading in indoor environments. However, the rate of increase is more gradual for the 2×2 array, indicating better link robustness at longer ranges. For example, at 3 meters, the single-element antenna suffers from a noticeable increase in PER, while the 2×2 array still maintains acceptable performance.

Fig. 16 presents the measured SINR results obtained from the OTA experiments using USRP platforms. The measurements reveal that the 2×2 array antenna consistently provides a higher SINR than the single-element antenna at all distances. This improvement is attributed to the array's higher gain and spatial diversity, which help to suppress interference and maintain stronger signal reception even as distance increases. At 0.7 GHz, the SINR starts above 28 dB for the 2×2 array and gradually decreases to about 18 dB at 3 meters, while the single-element antenna experiences a more pronounced drop from 25 dB to 10 dB. A similar trend is observed at 2.6 GHz, where the array maintains SINR above 16 dB, whereas the single-element antenna falls below 8 dB at longer distances.

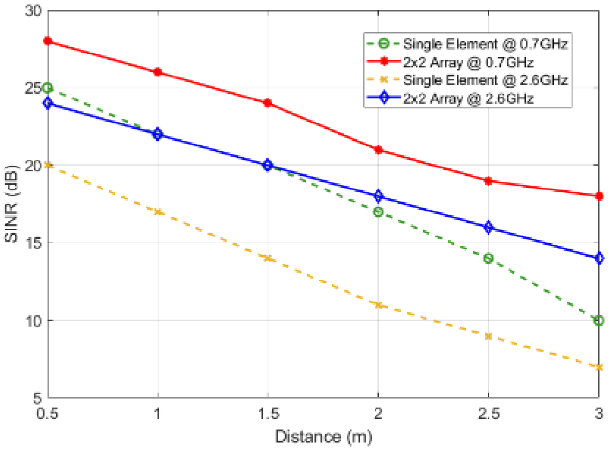

Fig. 16. Measured SINR as a function of transmission distance at 0.7 and 2.6 GHz for both the single-element and 2×2 antenna configurations.

Overall, the combination of low PER and high SINR across short-to-medium distances supports the suitability of the proposed antenna array for reliable low-power 5G medical communication in confined indoor environments.

It should be noted that radiation efficiency in this work was primarily obtained from CST simulations, as direct measurement methods such as Wheeler cap or anechoic chamber setups were not available in our laboratory. Instead, Over-the-Air (OTA) link testing with USRP platforms was performed at 0.7 and 2.6 GHz to provide indirect system-level validation. The measured Packet Error Rate (PER) and Signal-to-Interference-Plus-Noise Ratio (SINR) trends closely matched the simulated efficiency values, thereby providing indirect validation that the proposed antenna delivers sufficient effective radiated power for reliable communication. At the same time, OTA validation at 26 GHz was not possible due to hardware limitations of the available USRP platform, which lacks mmWave front ends. While simulations predict consistent impedance matching, stable gain, and radiation efficiency above 50% at 26 GHz, practical mmWave deployment is expected to encounter additional challenges such as higher path loss, multipath fading, and sensitivity to alignment. Future work will incorporate chamber-based efficiency measurements and mmWave-capable hardware to experimentally validate the 26 GHz performance and complete the full tri-band evaluation.

Table V presents a quantitative comparison between the proposed antenna and representative multi-band antenna designs reported in recent literature. While several prior works demonstrate high gain and radiation efficiency, particularly at mmWave frequencies [19–21], these designs are typically limited to microwave or mmWave-only operation and do not include experimental Over-the-Air (OTA) link validation.

TABLE V. QUANTITATIVE PERFORMANCE COMPARISON

Work	**Bands**	**Peak Gain (dBi)**	**Efficiency (%)**	**OTA Validation**
Proposed T-F Tri-band Array (This Work)	0.7 GHz (sub-GHz), 2.6 GHz (sub-6), 26 GHz (mmWave)	3.9–5.4	60–75	Yes PER & SINR
[19]	Sub-6 GHz (2–7 GHz), Ku (13–17.5 GHz), mmWave (24.5–38.2 GHz)	8–11	70–87	No
[20]	Microwave (2.6–4.1, 5.3–11.3 GHz), mmWave (22.5–29.3 GHz)	Up to 11	70–87	No
[21]	mmWave: 27.8, 32.0, 37.4 GHz	not reported	not reported	No
[22]	Sub-6 GHz tri-band (~0.9, 2.4, 3.5–5.8 GHz)	~4	<60	No
[23]	3.5, 26 GHz	3.8 / 7.5	74–86	No
[24]	28 & 38 GHz	4.6–5.9	78–90	No

Recent hybrid sub-6 GHz and mmWave antennas implemented on FR-4 substrates, such as the work in Ref. [23], report competitive gain and efficiency at both bands; however, they are restricted to dual-band operation and lack system-level communication evaluation. Similarly, medical and wearable mmWave antennas, exemplified by Ref. [24], achieve excellent radiation efficiency and SAR compliance at 28–38 GHz but do not support sub-GHz or sub-6 GHz connectivity and do not provide OTA reliability metrics.

In contrast, the proposed T–F shaped antenna uniquely combines sub-GHz, sub-6 GHz, and mmWave operation within a compact, low-cost FR-4 platform and provides experimental OTA validation using PER and SINR measurements. This system-level evaluation complements conventional antenna metrics and highlights the practical suitability of the proposed design for reliable 5G medical IoT communication in realistic indoor environments.

C. Discussion on mmWave Feasibility and Measurement Limitations

Although the proposed antenna is designed to operate at 26 GHz, experimental validation at the mmWave band was not performed in this work due to limitations of the available measurement hardware. The employed USRP platform does not support mmWave front-end operation, and access to a mmWave-capable VNA extension and anechoic chamber was not available during the experimental phase.

To assess the feasibility of mmWave operation, full-wave simulations were conducted in CST Microwave Studio, which predict stable impedance matching ($|S11| < -10$ dB), realized gain of approximately 3.9–4.2 dBi, and radiation efficiency of around 60% at 26 GHz. The reduced efficiency compared to sub-6 GHz bands is primarily attributed to the higher dielectric loss tangent of FR-4 at mmWave frequencies ($\tan \delta \approx 0.02$ at 26 GHz), increased conductor loss, and surface-wave excitation.

In practical measurements, additional degradation is expected due to fabrication tolerances, connector transitions, and surface roughness effects, which typically introduce an efficiency reduction of approximately 5–10%, as commonly observed in FR-4-based antennas operating at mmWave frequencies. Nevertheless, the simulated results suggest that the proposed T–F geometry can support short-range line-of-sight mmWave operation under controlled conditions.

Radiation efficiency in this work was primarily obtained from CST simulations, as direct measurement methods such as Wheeler cap or anechoic chamber-based efficiency testing were not available in the authors' laboratory. Instead, Over-the-Air (OTA) communication experiments were conducted at 0.7 and 2.6 GHz using USRP platforms.

The measured Packet Error Rate (PER) and Signal-to-Interference-plus-Noise Ratio (SINR) trends closely correlate with the simulated radiation efficiency and gain values, providing indirect but practical validation of the antenna's effective radiated performance. For instance, the proposed 2×2 array consistently achieved lower PER and higher SINR compared to the single-element antenna across all tested distances, confirming that the simulated efficiency translates into measurable system-level performance improvements.

Future work will include chamber-based radiation efficiency measurements and full OTA validation at 26 GHz using mmWave-capable hardware to complete the experimental assessment of the proposed tri-band antenna.

IV. DISCUSSION AND INTERPRETATION OF RESULTS

A. mmWave Performance Characteristics and Efficiency Trade-offs

The radiation efficiency of the proposed antenna exhibits a clear frequency-dependent trade-off between the sub-GHz and mmWave bands. At 0.7 GHz and 2.6 GHz, higher efficiency is achieved due to lower dielectric and conductor losses, as well as stronger near-field coupling between the radiator and the ground plane. In contrast, at 26 GHz, the efficiency decreases primarily because of the higher loss tangent of the FR-4 substrate, increased conductor loss, and surface-wave excitation. Despite this reduction, the achieved efficiency remains acceptable for short-range, line-of-sight medical IoT applications, where moderate gain and reliable connectivity are prioritized over long-range coverage.

At 26 GHz, the simulated Electric-field (E-field) distribution exhibits strong field concentration along the F-shaped branches of the radiator, particularly near the vertical stub and the shorted side arms. This behavior indicates that the mmWave resonance is primarily supported by localized higher-order modes, rather than the extended current paths responsible for sub-GHz and sub-6 GHz operation. Compared to lower-frequency bands, the E-field is more spatially confined to the radiating edges of the patch due to the shorter effective wavelength and reduced penetration depth at mmWave frequencies. This localized field behavior enables compact mmWave radiation without additional radiating elements or ground-plane modification, thereby preserving structural simplicity.

The simulated radiation pattern at 26 GHz exhibits a narrower main lobe and increased directivity compared to the sub-GHz and sub-6 GHz bands, as expected for electrically larger apertures at mmWave frequencies. Although secondary lobes are present, their levels remain sufficiently low for short-range line-of-sight communication scenarios. The realized gain of approximately 4 dBi at 26 GHz, together with stable impedance matching, suggests that the proposed antenna can support mmWave links in compact medical IoT devices, where directional coverage and short-range reliability are prioritized.

Despite the higher dielectric loss of the FR-4 substrate at mmWave frequencies, the simulated E-field and radiation characteristics indicate that the proposed geometry maintains acceptable performance at 26 GHz. This observation supports the feasibility of employing low-cost substrates for proof-of-concept tri-band medical communication systems, while more advanced low-loss substrates may further enhance mmWave efficiency in future implementations.

B. Estimated mmWave Link Budget for Indoor Medical Environments

To provide a system-level perspective on the feasibility of mmWave operation, an estimated link budget at 26 GHz was derived based on the same transmit power and baseband configuration used in the sub-6 GHz OTA experiments. A transmit power of +10 dBm and BPSK modulation at a data rate of 1 Mbps were assumed for this study, together with the simulated antenna gain of approximately 4 dBi at both the transmitter and receiver.

For a representative indoor medical environment with a transmitter–receiver separation of 3 m, the free-space path loss at 26 GHz is approximately 70 dB. Additional indoor attenuation due to furniture, partial human-body blockage, and multipath effects was conservatively estimated at 6 dB, resulting in a total path loss of approximately 76 dB. Under these conditions, the estimated received power is about −58 dBm.

Assuming a typical receiver sensitivity of approximately −80 dBm for BPSK at 1 Mbps, the resulting link margin is on the order of 20 dB. This margin suggests that the proposed antenna can support short-range mmWave communication in indoor medical environments under similar power and modulation assumptions to those used in the sub-6 GHz OTA measurements. It should be noted that this link budget represents an estimate based on idealized assumptions and is intended to provide qualitative insight into mmWave feasibility rather than a substitute for full experimental validation.

The extension of the single-element antenna into array configurations introduces additional trade-offs related to element spacing. In this work, the inter-element spacing was selected to be approximately $\lambda/2$ at 2.6 GHz, which provides a good balance between mutual coupling suppression and radiation efficiency in the mid-band. However, this physical spacing corresponds to a much larger electrical separation at 26 GHz, leading to narrower main beams and more pronounced side lobes. While not optimized for mmWave beamforming, this configuration is sufficient for proof-of-concept tri-band operation and highlights the challenges of achieving optimal array performance across widely separated frequency bands using a single geometry.

A comparison between simulated and measured results further confirms the validity of the proposed design. The measured S11 closely follows the simulated trends at all three operating bands, with minor frequency shifts and magnitude differences observed, particularly at the sub-GHz band. These deviations can be attributed to fabrication tolerances, SMA connector effects, soldering imperfections, and variations in the dielectric properties of FR-4. Despite these factors, the overall agreement between simulation and measurement demonstrates that the design methodology and modeling approach are reliable. The measured gain trends also align well with simulated predictions, confirming that the proposed antenna maintains consistent radiation characteristics when implemented in hardware, despite practical fabrication and measurement constraints.

V. CONCLUSION

This paper presented the design, optimization, and implementation of a compact tri-band patch antenna and its extension into a 2×2 array for 5G medical communication. The proposed antenna operates at 0.7 GHz, 2.6 GHz, and 26 GHz, covering both sub-6 GHz and mmWave bands within a compact, low-cost FR-4 platform. Simulation results demonstrated strong impedance matching ($|S11| < -10$ dB), stable gain, and satisfactory radiation efficiency across all operating bands. Among the evaluated configurations, the 2×2 array exhibited the most balanced overall performance.

A prototype was fabricated and experimentally validated through VNA and radiation pattern measurements, showing good agreement with simulation. Over-the-Air (OTA) testing using USRP further confirmed superior communication performance, with improved SINR and reduced PER compared to the single-element antenna. The fabricated 2×2 array employed a 4-to-1 power combiner and operated as a single-port corporate-fed structure; therefore, conventional multi-port MIMO metrics were not considered, and performance was evaluated in terms of impedance matching, gain, radiation efficiency, and OTA link reliability.

The results demonstrate that the proposed antenna is a practical candidate for integration into non-implantable, portable 5G medical IoT devices and patient-side communication gateways. Future work will focus on extending the proposed tri-band antenna toward more advanced medical IoT communication scenarios. In particular, hybrid beamforming techniques with phase control will be investigated at the mmWave band to enhance directivity, suppress side lobes, and improve link robustness in dynamic indoor medical environments. In addition, a full Multiple-Input Multiple-Output (MIMO) implementation will be explored to support spatial diversity and capacity enhancement, accompanied by mmWave-capable OTA testing using phased-array front-ends and anechoic chamber measurements. Finally, for wearable and body-proximate medical applications, future studies will include safety and compliance evaluations, such as Specific Absorption Rate (SAR) analysis and experimental validation, to ensure regulatory and biomedical safety requirements are satisfied.

CONFLICT OF INTEREST

The authors declare no conflict of interest.

AUTHOR CONTRIBUTIONS

Paleerat Wongchampa: Conceptualization, Funding acquisition, Investigation, Data curation, Methodology, Software, Validation, Visualization, and Writing, original draft; Lerson Kirasamuthranon: Investigation, Project administration, Supervision, Visualization, Validation, Writing, review, and editing; both authors had approved the final version.

FUNDING

This research was funded by College of Industrial Technology, King Mongkut's University of Technology North Bangkok (Grant No Res-CIT0264/2020).

REFERENCES

[1] A. Ahad, M. Tahir, and K. L. A. Yau, "5G-based smart healthcare network: Architecture, taxonomy, challenges and future research directions," *IEEE Access*, vol. 7, pp. 100747–100762, July 2019.

[2] S. Singh, "5G enabled network technology trends for smart healthcare systems," *5G Wireless Communication System in Healthcare Informatics*, pp. 29–43, March 2023.

[3] S. Hamid *et al.*, "Hybrid beamforming in massive MIMO for next-generation communication technology," *Sensors*, vol. 23, no. 16, pp. 1–13, August 2023.

[4] J. Zhang, X. Yu, and K. B. Letaief, "Hybrid beamforming for 5G and beyond millimeter-wave systems: A holistic view," *IEEE Open Journal of the Communications Society*, vol. 1, pp. 77–91, January 2020.

[5] R. Dilli, "Hybrid beamforming in 5G NR networks using multi user massive MIMO at FR2 frequency bands," *Wireless Personal Communications*, vol. 127, no. 4, pp. 3677–3709, September 2022.

[6] A. M. P. Ochoa *et al.*, "Smart healthcare applications over 5G networks: A systematic review," *Applied Sciences*, vol. 13, no. 3, 1469, January 2023.

[7] P. Popovski *et al.*, "5G wireless network slicing for EMBB, URLLC, and MMTC: A communication-theoretic view," *IEEE Access*, vol. 6, pp. 55765–55779, 2018.

[8] A. Moglia *et al.*, "5G in healthcare: From COVID-19 to future challenges," *IEEE Journal of Biomedical and Health Informatics*, vol. 26, no. 8, pp. 4187–4196, August 2022.

[9] A. Iqbal *et al.*, "Optimizing spectral utilization in healthcare internet of things," *Sensors*, vol. 25, no. 3, p. 615, January 2025.

[10] M. Islam *et al.*, "Development of smart healthcare monitoring system in IoT environment," *SN Computer Science*, vol. 1, no. 3, 2020.

[11] A. M. Vegni and V. Loscri, "A survey on vehicular social networks," *IEEE Communications Surveys and Tutorials*, vol. 17, no. 4, pp. 2397–2419, July 2015.

[12] 3GPP. TS 22.261 – Service Requirements for the 5G System; Stage 1. [Online]. Available: https://www.etsi.org/deliver/etsi_tr/121900_121999/121917/17.00.01_60/tr_121917v170001p.pdf

[13] 3GPP. TR 22.826 – Study on Communication for Automation in Vertical Domains. [Online]. Available: https://portal.3gpp.org/desktopmodules/Specifications/SpecificationDetails.aspx?specificationId=3546

[14] 3GPP. TR 22.862 – Feasibility Study on Smart Healthcare. [Online]. Available: https://portal.3gpp.org/desktopmodules/Specifications/SpecificationDetails.aspx?specificationId=3014

[15] N. K. Lee and N. K. F. Tong, "Microstrip patch antennas — Basic characteristics and some recent advances," *Proc. the IEEE*, vol. 100, no. 7, pp. 2169–2180, 2012.

[16] M. Alibakhshikenari *et al.*, "A comprehensive survey of metamaterial transmission-line based antennas: Design, challenges, and applications," *IEEE Access*, vol. 8, pp. 144778–144808, August 2020.

[17] S. A. Rahmani and H. Zerrouki, "Multi-slots microstrip patch antenna for 5G wireless communications," *Advances in Communication Technology, Computing and Engineering*, pp. 421–430, 2021.

[18] S. Rana and M. R. Smieee, "Design and analysis of microstrip patch antenna for 5G wireless communication systems," *Bulletin of Electrical Engineering and Informatics*, vol. 11, no. 6, pp. 3329–3337, October 2022.

[19] M. M. Rahman, S. Saha, and A. Mohan, "Three-dimensional tri-band 3×2 MIMO antenna array with wide bandwidth and isolation for sub-6 GHz, Ku-band, and mmWave applications," *Scientific Reports*, vol. 15, no. 1, pp. 12345–12356, Jan. 2025.

[20] M. M. Rahman, "Miniaturized tri-band integrated MIMO antenna loaded with metamaterial for microwave and millimeter-wave IoT applications," *Heliyon*, vol. 10, no. 2, e23456, Feb. 2024.

[21] P. Sharma and R. K. Chaudhary, "Flexible four-port tri-band MIMO antenna for FR2 mmWave 5G devices with SAR analysis," *Scientific Reports*, vol. 14, no. 1, pp. 7890–7902, Aug. 2024.

[22] H. Singh, "Compact Y-slot tri-band patch antenna with defected ground structure for sub-6 GHz 5G IoT systems," *Wireless Networks*, vol. 30, no. 7, pp. 15567–15578, Oct. 2024.

[23] S. Shamoon, W. Y. Zhou, F. Shahzad, W. Ali, and H. Subbyal, "Integrated sub-6 GHz and millimeter wave band antenna array modules for 5G smartphone applications," *AEU – International Journal of Electronics and Communications*, vol. 161, 2023.

[24] A. Salisu, U. Musa, U. U. Sabo, M. M. Abubakar, A. S. Hussaini, M. O. Akinsolu, C. H. See, and R. A. A. Alhameed, "Compact dual-band wearable antenna for millimeter-wave applications: Designed for medical and IoT device integration," *Progress in Electromagnetics Research Letters*, vol. 126, pp. 77–85, 2025.

[25] M. A. Rahman *et al*., "Metamaterial-based tri-band compact MIMO antenna," *Scientific Reports*, vol. 15, no. 1, pp. 1–22, 2025.

[26] E. M. Ali, H. Zhang, and Y. Chen, "Defected ground structure antenna array with metasurface for mmWave applications," *International Journal of Microwave and Wireless Technologies*, vol. 15, no. 1, pp. 1–14, 2025.

[27] A. Ullah, F. Khan, and T. Li, "Wideband coplanar waveguide MIMO antenna for 6G millimeter-wave applications with defected ground structure," arXiv preprint, arXiv:2508.08771, 2025.